The Presupernova Core Mass–Radius Relation of Massive Stars: Understanding Its Formation and Evolution

Alessandro Chieffi[1,2] and Marco Limongi[3,4]

[1] Istituto Nazionale di Astrofisica—Istituto di Astrofisica e Planetologia Spaziali, Via Fosso del Cavaliere 100, I-00133, Roma, Italy; alessandro.chieffi@inaf.it
[2] Monash Centre for Astrophysics (MoCA), School of Mathematical Sciences, Monash University, Victoria 3800, Australia
[3] Istituto Nazionale di Astrofisica—Osservatorio Astronomico di Roma, Via Frascati 33, I-00040, Monteporzio Catone, Italy; marco.limongi@inaf.it
[4] Kavli Institute for the Physics and Mathematics of the Universe (WPI), The University of Tokyo Institutes for Advanced Study, The University of Tokyo, Kashiwa, Chiba 277-8583, Japan

Abstract

We present a fine grid of solar metallicity models of massive stars (320 in the range $12 \leqslant M(M_\odot) \leqslant 27.95$), extending from the main sequence up to the onset of the collapse, in order to quantitatively determine how their compactness $\xi_{2.5}$, defined by O'Connor & Ott, scales with the carbon–oxygen core mass at the beginning of core collapse. We find a well defined, nonmonotonic (but not scattered) trend of the compactness with the carbon–oxygen core mass that is strictly (and mainly) correlated to the behavior, i.e., birth, growth, and disappearance, of the various carbon convective episodes that follow one another during the advanced evolutionary phases. Though both the mass size of the carbon–oxygen core and the amount of ^{12}C left by the central He burning play a major role in sculpting the final mass–radius relation, it is the abundance of ^{12}C that is ultimately responsible for the final degree of compactness of a star, because it controls the ability of the carbon-burning shell to advance in mass before the final collapse.

Supporting material: machine-readable table

1. Introduction

A proper understanding of the final fate of a massive star is mandatory to estimate some of the outcomes of its explosion, like, e.g., the mass of the remnant and the chemical composition of the ejecta. In order to reach such a goal, both the presupernova evolution and the following explosion must be properly simulated.

In the last decade, the large body of theoretical works devoted to the explosion of massive stars was mainly focused on the progressively more sophisticated treatment of the neutrino transport in multidimensional hydrodynamic simulations of core collapse. Given the enormous amount of literature on the subject, we refer the reader to the leading groups that currently explore the explosion of massive stars in 3D (Janka 2017; Müller et al. 2017; Burrows et al. 2019), and the references therein.

On the other hand, the presupernova evolution is also crucial because it determines some of the properties of a star at the onset of core collapse that drive the following explosion, like, e.g., the density profile (or, equivalently, the mass–radius (M–R) relation), the mass of the iron core, and its electron fraction (Y_e) profile (Cooperstein et al. 1984; Baron et al. 1985; Bethe 1990; O'Connor & Ott 2011, 2013). Such a final configuration is the result of the complex interplay between the nuclear burning and the number, timing, and overlap of the various convective zones. In this context, one of the key uncertainties connected with this complex behavior is the treatment of the various instabilities (thermal, rotation induced, etc.) that, in most cases, are still simulated very crudely by means of the Schwarzschild/Ledoux criterion, the mixing length theory, the presence/absence of convective overshooting, the parameterized efficiency of semiconvection, and so on. Given the large variety of different possible choices it is clear

that the final structure of a star may depend, even significantly depend, on the choices adopted by each author/group. Moreover, most of the computations presently available usually present results with a step in mass of at least half a solar mass or more (our typical step is of the order of a few solar masses). However, in recent years the situation changed substantially because Sukhbold & Woosley (2014) and Sukhbold et al. (2018) started a detailed study of the evolution of massive stars and their associated explosions by adopting a very fine step in mass ($\Delta M = 0.01\ M_\odot$). Among the various results presented in these papers, an interesting outcome highlighted by the authors is that even minor changes in the initial mass of a star may lead to very different structures at the beginning of the collapse. Such strong variations in the density profile are readily visible by taking advantage of a parameter, first introduced by O'Connor & Ott (2011), that summarizes the compactness of a star by means of a single parameter ξ, which is just the ratio between the mass M and its corresponding radius R at the mass location $M = 2.5\ M_\odot$, i.e., $\xi_{2.5} = 2.5\ M_\odot / R_{2.5}$ (1000 km). Figure 8 in Sukhbold et al. (2018) shows exactly such a result. In particular between 14–20 $M_\odot$ and between 22–24 $M_\odot$ a large scatter in the compactness of the models is evident.

Since our first paper on the subject (Chieffi et al. 1998) we have addressed many aspects of the evolution of the massive stars in a wide mass range (typically in the range 11–120 $M_\odot$) and metallicity (0 to solar) (Limongi & Chieffi 2012) and also various initial rotation velocities (Limongi & Chieffi 2018). Our typical step in mass has always been of the order of 1 solar mass or more. Given the relevant implications of the results obtained by Sukhbold and coauthors, we consider of great interest that we compute, show, and discuss the trend we obtain for the ξ parameter as a function of the initial mass with a mass step much smaller than used in our previous computations.

Table 1
Network

Isotope	Isotope
^{1}H	^{24}Mg
^{2}H	^{28}Si
^{3}He	^{23}Na
^{4}He	^{31}P
^{7}Li	^{32}S
^{7}Be	^{36}Ar
^{12}C	^{40}Ca
^{13}C	^{44}Ca
^{13}N	^{44}Ti
^{14}N	^{48}Ti
^{15}N	^{48}Cr
^{15}O	^{52}Cr
^{16}O	^{52}Fe
^{17}O	^{56}Ni
^{17}F	^{56}Fe
^{20}Ne	

We will not attempt any connection between compactness and explodability because it is both beyond the purposes of the present study and also because it has often been criticized. Ertl et al. (2016), for example, proposed the adoption of two parameters to infer the possible explodability of a stellar model: the mass location, and its derivative, with respect to the radius evaluated at the coordinate where the entropy per nucleon reaches a value of 4 (which basically corresponds to the base of the O-burning shell). We refer the reader to that paper for more details. Also, Burrows et al. (2019) regard the use of the compactness ξ to infer the explodability of a model as unreliable.

The paper is organized as follows. The version of the code adopted for this analysis is presented in Section 2, while the properties of all our models are discussed in detail in Section 3. Section 4 is devoted to a comparison between some of our results and those presented by Sukhbold et al. (2018). A final conclusion summarizes our results.

2. The Models

All the models discussed in this paper have been computed with the FRANEC evolutionary code, release 6. This version is the same used in Limongi & Chieffi (2018), with the exception of the nuclear network and the number of mesh points. In this set of computations we adopted a reduced network (shown in Table 1) because we were basically interested in the physical evolution of the models, and not in the detailed nucleosynthesis, but also because the calculation of this very large grid of models with our full network would have required an unfeasible amount of computer time. However, in order to check the consequences of this choice, we computed four models with the full network and found that the final compactness ξ (the main property we are interested in this study) closely resembles the one obtained with the small network (see Section 4). The number of mesh points has been slightly increased so that they now range between 2000 and 6000 (apart from the outermost 1% of the mass, i.e., the envelope, which is described by a few hundred mesh points), depending on the mass and the evolutionary phase. A great effort was devoted to choosing a mesh distribution refined enough to provide a very clean temporal evolution of the central He burning, in order to avoid the spurious ingestion of

fresh He toward the end of the He burning and hence give a random scatter in the final C abundance. To be more specific, FRANEC adopts several strategies in the mesh distribution: in addition to the classical requirements that the various variables, radius, luminosity, pressure, temperature, mass, and the main nuclear species do not vary by more than a specific amount that depends on the initial mass, current mass, and evolutionary phase, we also identify the regions where the difference between the adiabatic and radiative gradients is smaller than a given amount (usually 0.1). In these regions new meshes may be inserted but not removed. Another important strategy that we already included a long time ago is that FRANEC automatically adds additional meshes before they are really needed: for example when a low mass star climbs along the red giant branch, strong gradients of both pressure and temperature form within the H-burning shell so that a relatively large number of meshes is required to properly describe the burning shell. Similarly, above the H-burning shell all the variables vary much more smoothly and the number of meshes reduces. In this condition, FRANEC anticipates the arrival of the burning shell by substantially increasing the number of meshes in a region of the order of twice the mass of the burning shell.

Figure 1 (left) shows the run of the central C abundance left by the core He burning as a function of the initial mass (red dots). A scatter, even modest, in the C abundance would spoil all of the following advanced burning (because of the tremendous importance of the C abundance in driving all of the advanced evolutionary phases) and therefore it would eliminate all of the efforts to produce a clean starting point for the advanced burning. Our grid of models consists of 320 evolutionary tracks in the range 12–27.95 $M_\odot$ with a step in mass of 0.05 $M_\odot$. We adopted the solar metallicity of Asplund et al. (2009) ($Z = 1.345 \times 10^{-2}$), a He abundance equal to $Y = 0.265$, and a mixing length parameter $\alpha = 2.1$. Table 2 shows some relevant data of the models presented here. Columns 1–6 show, respectively, the initial mass, the final values of the total mass, the He core mass, the CO core mass, the Fe core mass, all in solar masses, and the fraction of C12 left by the central He burning. The last two columns show the final compactness ξ evaluated for the CO core mass and 2.5 $M_\odot$. All models were evolved up to a central temperature of $\sim$8 GK. For the sake of clarity let us explicitly mention that we define (a) the end of central He burning as the time at which the central abundance of He drops to a mass fraction of 10^{-8}, and (b) the mass of the CO core as the mass coordinate where the tail of the He profile drops below a mass fraction of 10^{-3}. Let us eventually note that the current value of the mixing length parameter we adopt was fixed a few years ago when we turned to the solar distribution of Asplund et al. (2009). Such a change forced us to recalibrate the mixing length parameter. Our calibration is obtained by requiring that a star of 1 $M_\odot$, after 4.57×10^9 yr of evolution, reaches the current solar luminosity ($L_\odot = 3.826 \times 10^{33}$ erg s^{-1}) and radius $R_\odot = 6.951 \times 10^{10}$ cm. Over the years our calibration of α changed from 1.6, to 2.25 and now 2.1, the value depending on the opacities and the solar chemical composition adopted.

3. Discussion

The advanced burning phases of a massive star, i.e., those going from central He exhaustion up to the onset of core collapse, are determined once both the CO core mass (M_{CO}) and the mass fraction of ^{12}C($X(^{12}$C)) left by the central He
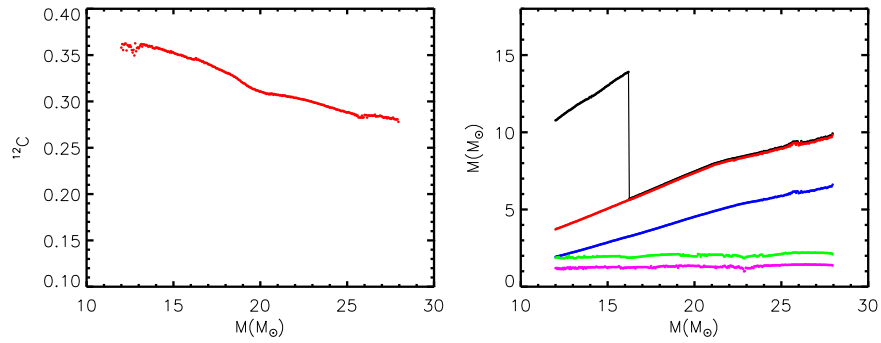
Figure 1. (Left) C mass fraction left by the He burning; (right) total mass (black), He core mass (red), CO core mass (blue), O-burning shell mass (green), and Si-burning shell mass (magenta). The O- and Si-burning shells have been shifted by $+0.03\ M_\odot$ and $-0.03\ M_\odot$, respectively, to improve readability.

burning are known. This means that while the H- and the He-burning phases may be considered as monoparametric, in the sense that they are controlled by a single parameter (the current mass or the He core mass), the advanced burning requires the simultaneous knowledge of M_{CO} and $X(^{12}C)$ in order to be uniquely determined and may therefore be considered biparametric. The CO core mass is fundamental because it plays the role the total mass has in central H burning and the He core mass has in He burning, while the ^{12}C left by the He burning determines the amount of fuel available to the C burning and hence determines the number and the extension (in mass) of the various C convective episodes. Both contribute to shaping the M–R relation at the onset of core collapse and hence controlling the development of all other burning and of the Fe core mass. Figure 1 (right) shows the run of the CO core mass (blue dots) as a function of the initial mass for all our 320 models. For the sake of completeness, the same panel also shows the run of the total mass (black dots plus line), the He core mass (red dots), the O-burning shell mass (green dots), and the Si-burning shell mass (magenta dots) with the initial mass. The vertical drop in the total mass occurring at $M = 16.25\ M_\odot$ marks the transition between the masses that experience vigorous mass loss due to dust formation (van Loon et al. 2005), $M \geqslant 16.25\ M_\odot$, and those that do not. Of course, this sharp transition also separates the stars that explode as red supergiants from those that turn blue before the final explosion. All four relations show a very tight dependence on the initial mass with basically no scatter.

In order to understand the scaling of the compactness of stars with the initial mass at the onset of core collapse, it is first necessary to fix an operational definition of the compactness of a star and then understand how it changes during its evolution. The natural relation that fully describes the compactness of a star in any evolutionary phase is the M–R relation (or, equivalently, the density profile). Figure 2 shows, as an example, the M–R relation of a 15 $M_\odot$ star at various key evolutionary phases: the black line refers to the end of the central He burning, while the red, green, blue, magenta, and cyan lines mark, the beginning and the end of the central C burning, the end of the central Ne and O burning, and the last model, respectively. The dark green dot marks the position of the O-burning shell (which practically coincides with the location where the entropy per baryon S is equal to 4 in units of Boltzmann constant) while the dark red dot marks the position of the C-burning shell. The black horizontal line marks the mass coordinate of the CO core. Incidentally, the mass of the CO core is fixed as soon as the He convective shell forms. The reason is that from this moment on, the He-burning shell cannot advance any more in mass because it is continuously fed fresh

fuel from the convective shell. The smooth, shallow, M–R profile left by the He burning progressively steepens and a knee begins to appear as soon as an efficient burning shell forms. The main burning shell that controls the position and the bending of the knee just before the collapse is the O-burning shell, which is readily visible in Figure 2. This figure may be considered a template since the M–R relation of any massive star shows a similar shape at the onset of core collapse. Though this relation fully describes the compactness of a star, it is clear that it is not possible to compare the final M–R relations of all of our 320 models in a single plot to determine their scaling with the initial mass. Therefore, we decided to compare the compactness of some selected layers. In analogy with the strategy adopted by, e.g., O'Connor & Ott (2011), we chose to define the compactness of any mass coordinate "M_i" by means of the operational ratio $\xi_{(i)} = M_i(M_\odot)/R_i(1000\ km)$. The first relevant mass location worth analyzing is the one corresponding to the the CO core, for which the compactness is defined as $\xi_{CO} = M_{CO}(M_\odot)/R_{CO}(1000\ km)$. The black dots in Figure 3 show the run of ξ_{CO} with the initial mass soon after the formation of the CO core. At this stage, a tight monotonic relation between the compactness of the CO core and the initial mass exists. The moderate increase of the M/R ratio with M is what one would qualitatively expect on the basis of dimensional arguments. In fact, a gas cloud in hydrostatic equilibrium has an M/R roughly constant if the equation of state (EOS) is dominated by the particles, while it scales as $M^{1/2}$ if the EOS is dominated by photons. In a mixed case in which both particles and photons contribute significantly to the EOS, we expect a direct scaling of M/R with M. Full integration of the stellar equations confirms this qualitative expectation. This trend is not qualitatively modified by the central C burning, the only difference being an increase of the overall compactness of the CO core mass as a consequence of the natural continuous contraction of the core. Therefore, at the end of the central C burning the scaling of ξ_{CO} with the mass is still tight and (almost) monotonic (red dots in Figure 3).

The (almost) monotonic relation between ξ_{CO} and the initial mass disappears in the passage from the end of the central C burning to the beginning of the central Ne burning (green dots in Figure 3). Though the correlation between the compactness of ξ_{CO} and the initial mass is still very tight, some features begin to appear. On average ξ_{CO} still increases with the initial mass, but now a jump forms at $M_{ini} = 15.75\ M_\odot$, a minimum is present at $M_{ini} = 22.8\ M_\odot$, and a turn over occurs above 25 $M_\odot$. The formation of these features reflects the different evolution of the C convective shells as the initial mass increases.

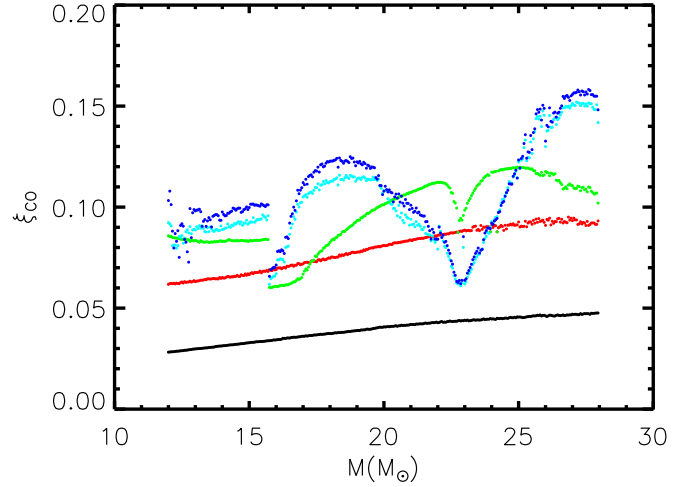<div align="center">

Table 2
Main Data

</div>

M_{ini} $M_\odot$	M_{fin} $M_\odot$	M_{He} $M_\odot$	M_{CO} $M_\odot$	M_{Fe} $M_\odot$	^{12}C Mass Fraction	ξ_{CO} $M_\odot/R(10^3 \text{ km})$	$\xi_{2.5}$ $M_\odot/R(10^3 \text{ km})$
12.00	10.7738	3.7111	2.1955	1.5001	0.3581	0.0721	0.0290
12.05	10.8002	3.7455	2.2161	1.5159	0.3619	0.0741	0.0309
12.10	10.8379	3.7689	2.2358	1.4475	0.3555	0.0709	0.0321
12.15	10.8922	3.7818	2.2412	1.5131	0.3611	0.0642	0.0310
12.20	10.9366	3.8001	2.2530	1.4402	0.3623	0.0595	0.0307
12.25	10.9767	3.8226	2.2685	1.4892	0.3625	0.0636	0.0330
12.30	11.0095	3.8510	2.2878	1.4419	0.3550	0.0615	0.0341
12.35	11.0641	3.8600	2.2942	1.4434	0.3608	0.0642	0.0354
12.40	11.1107	3.8818	2.3052	1.5078	0.3603	0.0572	0.0341
12.45	11.1369	3.9135	2.3272	1.4216	0.3590	0.0658	0.0392

(This table is available in its entirety in machine-readable form.)
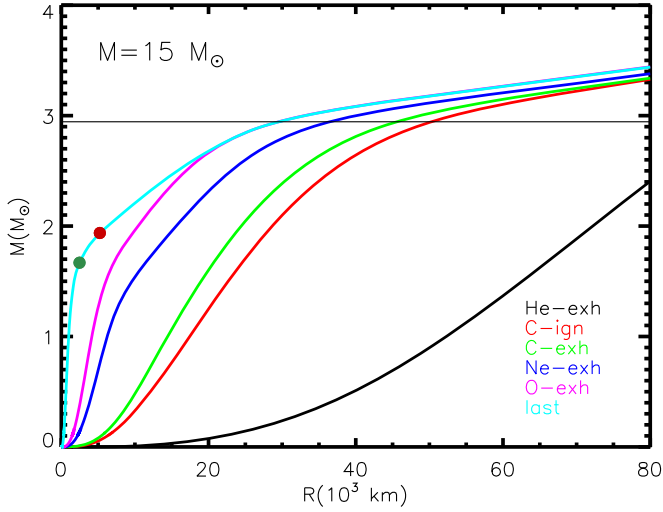
Figure 2. M–R relation of a 15 $M_\odot$ star of solar metallicity at different phases: He ignition (black), C ignition (red), C exhaustion (green), Ne exhaustion (blue), O exhaustion (magenta), and last model (cyan). The dark green and dark red dots mark the bases of the O- and the C-burning shells in the last model, respectively. The thin black horizontal line shows the CO mass.

Figure 3. Compactness of the CO core mass at various evolutionary phases: central He exhaustion (black), central C exhaustion (red), central Ne ignition (green), central Si exhaustion (cyan), and last model (blue).

For the sake of clarity let us remember that the advances in mass of the C-burning shell are characterized by the formation of a few (usually two/three in this mass interval) convective shell episodes. The growth of these thermal instabilities has two major effects: on one hand they halt (or at least slow down) the advancing of the burning shell because they continuously feed it with fresh fuel (until the convective region is rich in fuel) and, on the other hand, they determine a more or less effective expansion of part of the overlying layers, softening therefore their compactness, i.e., their ξ, until they are active.

Figure 4(a) shows the Kippenhahn diagram and the run of both ξ_{CO} and the central temperature (red and blue lines in (d)) of 12 $M_\odot$. A comparison between these two panels clearly shows that the formation of the convective core slows down the contraction of the core as well as its heating. The formation of the first convective shell initially leads to an expansion of the CO core (ξ_{CO} decreases). The same holds for the second C convective shell. Only after the exhaustion of the second convective shell is the inner core massive enough to be able to contract and heat up to the temperature necessary for the Ne photodisintegration. In fact, the Ne convective core (located at $\log_{10}(t - t_{fin}) \sim 0.8$) forms some time after the disappearance

of the second C convective shell (Figure 4). This behavior remains qualitatively unaltered up to 15.70 $M_\odot$: Figures 4(b) and (e) show the same quantities as plotted for 12 $M_\odot$, but for 15.70 $M_\odot$. Above this threshold mass the evolution between the end of the central C burning and the Ne ignition changes drastically, because the C-exhausted core at the time of the disappearance of the first C convective shell is massive enough to contract and heat up, independently of the behavior of the second C-burning shell. The faster contraction of the inner core forces the second C convective shell to ignite more violently than in the less massive stars, and such a large injection of energy forces the outer layers to expand, including the border of the CO core: this is the reason for the sharp decrease of ξ_{CO} at $M = 15.75 M_\odot$. Figures 4(c) and (f) show such a change of behavior for 15.75 $M_\odot$. Figure 5 shows, even more clearly, how the contraction timescale of the CO core changes with the initial mass. Stars in the range 12–15.70 $M_\odot$ show a temporary temperature decrease (a hook) during the activity of the second C convective shell while the more massive stars contract and heat without experiencing any delay in the heating of the inner core.

Stars in a range from 15.75 $M_\odot$ to roughly 17 $M_\odot$ reach Ne ignition with ξ_{CO} smaller (i.e., a more expanded CO core) than the one they had at the end of the central C burning because of the power of the second convective shell. But, as the initial
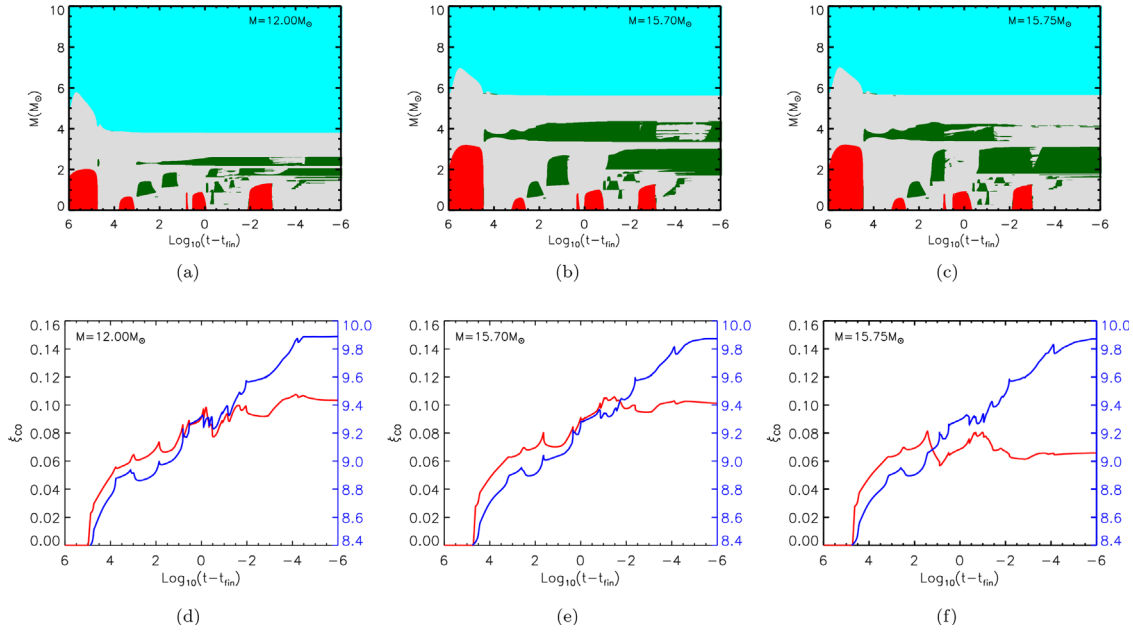
Figure 4. (a)–(c) Kippenhahn diagrams of the 12, 15.70, and 15.75 $M_\odot$ models. The red, cyan, and green areas mark the convective core, the convective envelope, and the convective shells, respectively. The blue line, when present, refers to the current mass of the star. Time is counted from the collapse time. (d)–(f) Temporal run of the central temperature (blue) and of the compactness of the CO core mass (red). Each lower panel refers to the same mass shown in its corresponding upper panel.
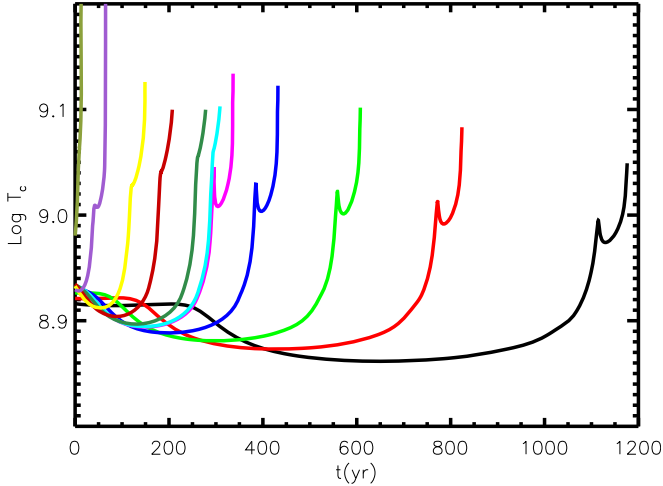

Figure 5. Temporal evolution of the central temperature for a subset of models. Time starts from the end of the central He burning. The various lines refer to the 12 $M_\odot$ (black), 13 $M_\odot$ (red), 14 $M_\odot$ (light green), 15 $M_\odot$ (blue), 15.7 $M_\odot$ (magenta), 15.75 $M_\odot$ (cyan), 16 $M_\odot$ (dark green), 17 $M_\odot$ (dark red), 18 $M_\odot$ (yellow), 20 $M_\odot$ (purple), and 27 $M_\odot$ (gray) models, respectively.

mass increases, the second C convective shell weakens progressively and even vanishes before Ne ignites, so the CO core has time to contract further by the time the center reaches the Ne-burning condition. The net consequence is a progressive increase of ξ_{CO}. This effect is readily visible in Figure 6, where the Kippenhahn diagrams of the 18, 20, and 22 $M_\odot$ models are shown together with the temporal evolution of both ξ_{CO} and central temperature: the size of the second C convective shell progressively reduces when moving from the 18 to the 22 $M_\odot$ models, while the Ne ignition shifts toward later times with respect to the end of the second C convective shell. Above ~22 $M_\odot$, ξ_{CO} inverts its trend with the initial mass: the early formation of the third C convective shell is responsible for this turn down. Up to now we have not mentioned the third convective shell because it forms after the Ne burning in masses

smaller than ~22 $M_\odot$. The systematic decrease of the power of the second C convective shell as the initial mass increases speeds up the contraction and heating of the CO core so that the formation of the third convective shell progressively occurs earlier and earlier in time, and around 22 $M_\odot$ its formation almost coincides with Ne ignition. Similarly to what happens around 15.7 $M_\odot$, the growth of this convective shell forces the overlying layers to expand and hence ξ_{CO} to decrease. The right panels in Figure 6 show that at the beginning of the Ne burning ($\log(t - t_{end}) \sim -0.02$), ξ_{CO} begins to drop because of the growth of the third convective shell. In the mass range 22–22.9 $M_\odot$, the third C convective shell systematically forms before the central Ne ignition and this occurrence leads to a progressive decrease of ξ_{CO} in this mass interval. As the initial mass continues to increase (above ~22.9 $M_\odot$), the strength of the third C convective shell also progressively weakens and, accordingly, ξ_{CO} increases again. The behavior of the third C convective shell is well summarized in Figure 7 where the same quantities plotted for the less massive stars are now shown for the 23, 24, 25, and 26 $M_\odot$ models.

The cyan dots in Figure 3 show the trend of ξ_{CO} at the central Si exhaustion. It is worth noting that the main features already present at the Ne ignition are still there, i.e., the discontinuity at 15.75 $M_\odot$ and the minimum at 22.8 $M_\odot$. In addition to this, it is worth noting that while the CO cores of stars in the intervals 12–20 $M_\odot$ and 25–27.95 $M_\odot$ show a more compact structure with respect to the ones they have at the central Ne ignition (because they tend on average to contract as the center evolves), stars in the range 20–25 $M_\odot$ show the opposite behavior, reaching the end of the central Si burning with a CO core more expanded than at the central Ne ignition: the reason is that this is the mass interval in which the third C convective shell reaches its maximum strength and extension, and we have already seen before that a very strong burning shell forces the overlying layers to expand and hence to reduce their compactness. The lower panels in Figures 4, 6, and 7 clearly show that the compactness of the CO core does not increase
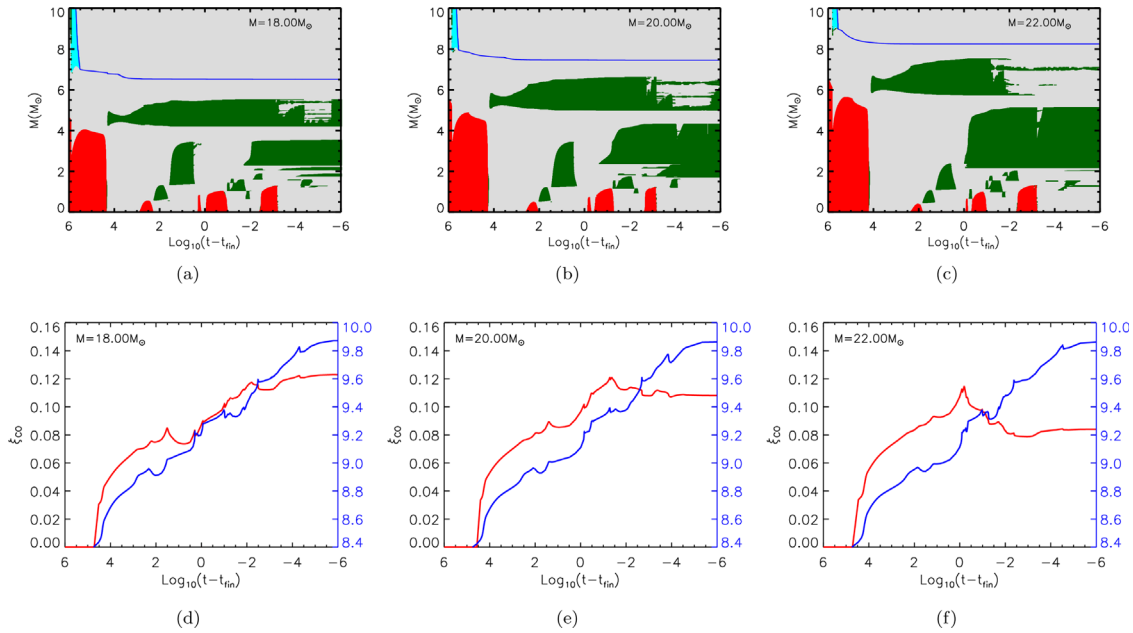
Figure 6. Same as in Figure 4, but for the 18, 20, and 22 $M_\odot$ models.

any more (but it can decrease) after the formation of the last C convective shell. The small drop (and scatter) in ξ_{CO} that is present at ~26 $M_\odot$ in Figure 3 is due to the formation of a small He convective shell (in the tail of the He profile) that merges with the main one. The sudden shift of the base of the new wider He convective shell to a more internal mass coordinate obviously forces also a jump of ξ_{CO}. The blue dots in Figure 3 show the final compactness of the CO cores of our models at the onset of the core collapse. With respect to the end of the central Si burning, there is now only a modest or even negligible variation of the compactness of the CO core mass. A final thing worth noting is that even if the trend of ξ_{CO} with the initial mass is not monotonic, the correlation is extremely tight, and there is basically no scatter of the points (no chaotic behavior) around the average trend line.

The second mass location that is worth discussing is the one corresponding to 2.5 $M_\odot$. The reason being that this mass location has been used (O'Connor & Ott 2011, 2013; Sukhbold & Woosley 2014; Sukhbold et al. 2018) as a proxy for the explodability of a model. Though we do not discuss the connection between compactness and explodability in this paper, we think it would be interesting to show and discuss the compactness of this layer that, in a large fraction of the models in the present grid ($14.00 \leqslant M\,(M_\odot) \leqslant 24.25$), is located within the last, most extended, C convective shell. Figure 8 shows the run of $\xi_{2.5}$ at some selected phases: the end of the central C burning (red dots), the beginning of the Ne photodisintegration (green dots), the end of the central Si burning (cyan dots), and the last model (blue dots). All the trends plotted in this figure show features that are strongly related to the ones already discussed for ξ_{CO} (Figure 3) and therefore they are also tied to the behavior of the C-burning shell. The scaling with the initial mass is still clean up to the end of the central C burning, while the various features begin to appear in the passage from the end of the central C burning to the Ne ignition. The evolution beyond the Ne burning amplifies the features already present at the central Ne ignition. The discontinuity present at ~20 $M_\odot$ at the onset of the collapse

marks the minimum mass in which a powerful third C convective shell forms (Figures 6(b) and (e)).

The third mass location worth presenting is the compactness of the knee present in the final M–R relation. Such a knee is sculpted by the O-burning shell that is located roughly at 1.7 $M_\odot$ (±0.2 $M_\odot$) in the mass interval discussed in this paper. We therefore chose this mass location to determine the compactness of the knee. Figure 9 shows the run of ξ_{knee} (green dots) together with the $\xi_{2.5}$ (black dots). Once again the main features shown by ξ_{knee} are the same as discussed above, and this reinforces the idea that the general trend of the compactness of a star as a function of the initial mass is dictated by the ability of the C burning to form powerful convective shells and to advance in mass.

There is, however, a third set of points in Figure 9. The blue dots show the trend of $\xi_{1.5}$, i.e., the compactness of layers that fairly well represent the average location of the Fe core of the present set of models. In this case, there is practically no trend with the initial mass and this is due to the fact that toward the end of their hydrostatic evolution, massive stars tend to share a similar M–R relation behind the Si shell.

4. Comparison with Similar Computations

The scaling of the compactness of massive stars with the initial mass has been discussed in several papers (see Section 1); one of the most extensive studies on this subject published to date is the one by Sukhbold et al. (2018; hereafter SWH18). One of the key results of that paper (already found in previous ones of the same series) is that the final compactness of the stars shows a significant scatter around the main trend in at least some mass intervals. The authors interpret this result as an intrinsic property of these stellar models because their evolution is "statistical in nature." Given the relevance of the final compactness of a star at the onset of the core collapse because of its intimate connection to the possible success/failure of the explosion, it is useful to compare their results to ours and to briefly comment on them.
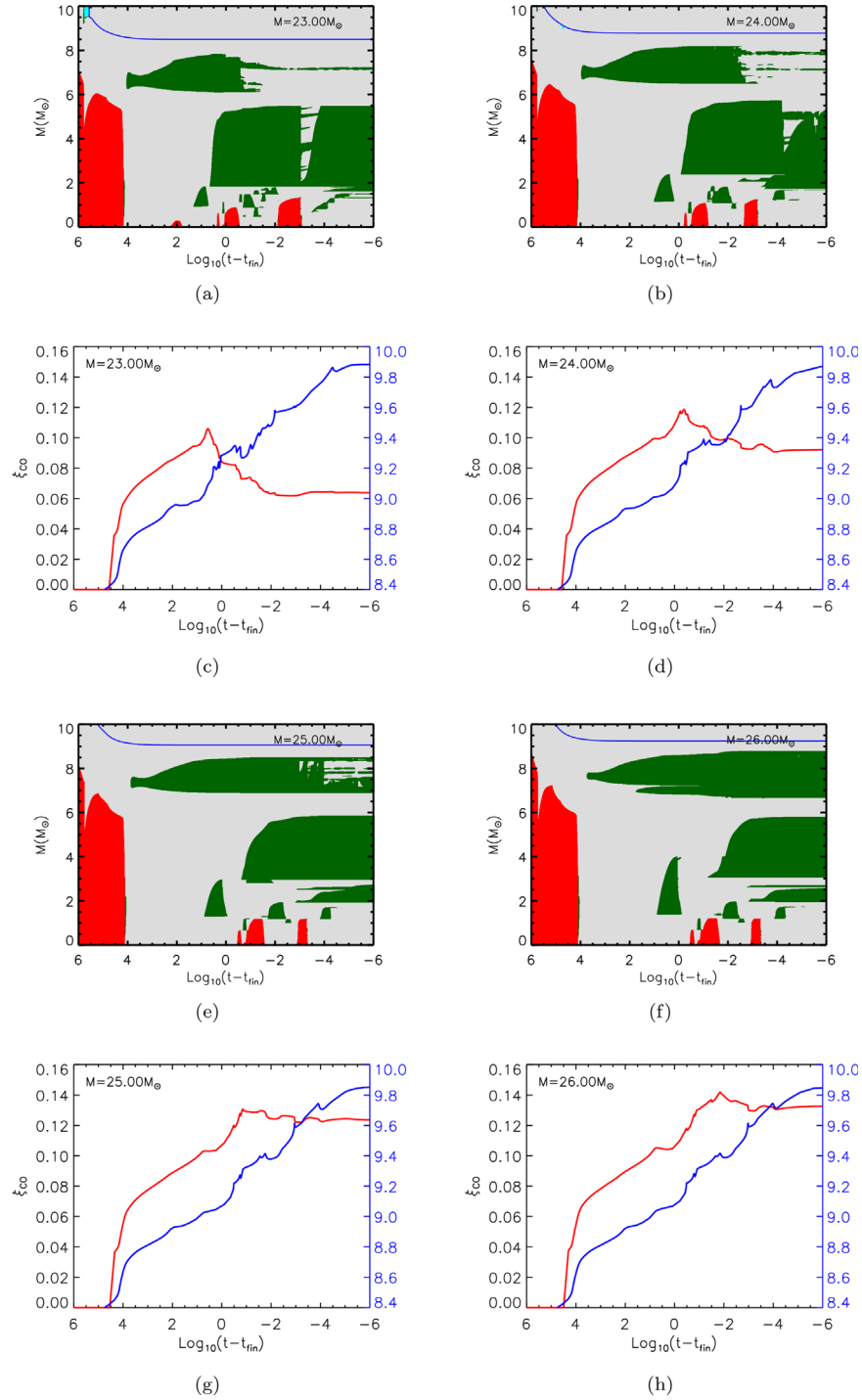
Figure 7. Same as in Figure 4, but for the 23, 24, 25, and 26 $M_\odot$ models.

Figure 10 shows the comparison between some key properties of our models and those published by SWH18. Panel (a) shows the run of the ^{12}C mass fraction left by He burning with the initial mass, the red and blue dots referring to our and SWH18's models, respectively. It is evident that a quite large offset exists between the two sets of models. Since the evolution of a star in central He burning (and beyond) is largely controlled by its He core mass, and not the total mass, Figure 10(c) shows the same comparison as a function of the He core mass. This panel is particularly robust because the conversion of C in O occurs toward the end of the He burning,

and since the final abundance of O scales directly with the central temperature (and hence with the He core mass), the final C/O ratio is largely fixed by the current value of the He core mass toward the end of the He burning, and not by the previous history of the star. For example, stars computed with or without mass loss are expected to lie basically on the same line in this kind of graph. The parameters that really control the final abundance of ^{12}C (for any fixed value of the He core mass) are the nuclear reaction rates of 3α and ^{12}C$(\alpha,\gamma)^{16}$O, i.e., their nuclear cross sections times the behavior of the convective core toward the end of the He burning (Imbriani et al. 2001). The
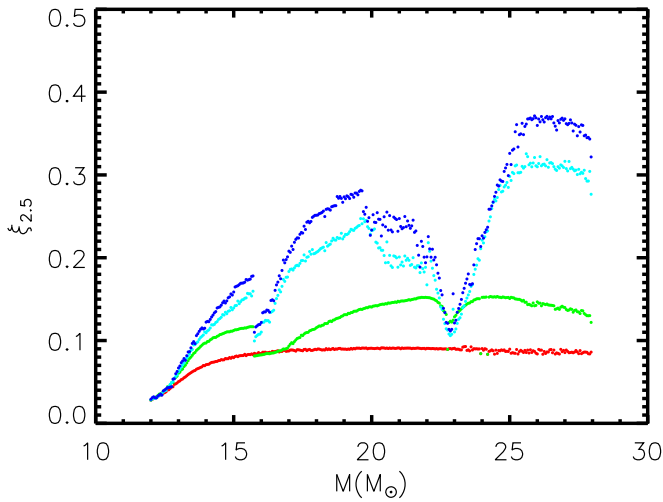
Figure 8. Compactness of the mass coordinate 2.5 $M_\odot$ at various phases: end of the central C burning (red), central Ne ignition (green), central Si exhaustion (cyan), and the last model (blue).
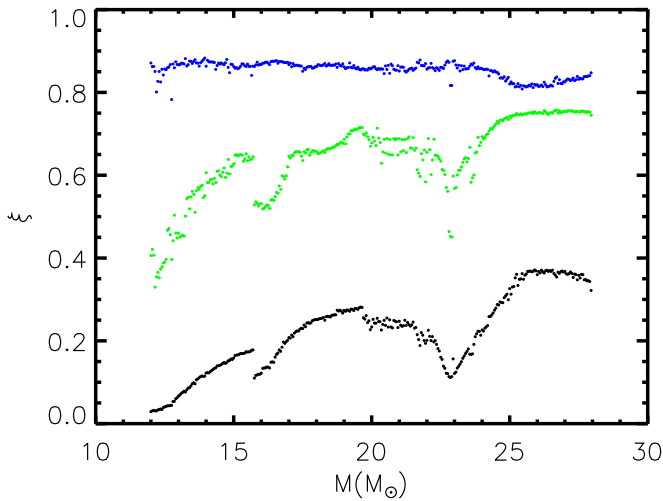

Figure 9. Final compactness of the models for three different mass coordinates: 2.5 $M_\odot$ (black), base of the O-burning shell (green), and the Fe core mass (blue).

offset between the two sets of computations visible in Figure 10(a) remains basically unaltered in panel (c). Though both sets of models adopt the same (NACRE; Angulo et al. 1999) nuclear cross section for 3α, the nuclear cross section adopted for $^{12}C(\alpha,\gamma)^{16}O$ is slightly different (we adopt Kunz et al. 2002, while SWH18 adopt 1.2 times Buchmann 1996, 1997, hereafter BU961p2). In order to check the role played by the two different nuclear cross sections on the ashes of the He burning, we have recomputed three models (15, 20, and 27 $M_\odot$) by adopting the BU961p2 nuclear cross section. The magenta dots in Figure 10(c) refer to these test models: it is quite evident that at most one third of the offset may be due to the adoption of the two different nuclear cross sections. In our opinion, the large offset is probably due to a substantial difference in the treatment of the border of the convective core in central He burning. A hint toward this explanation comes from Figure 10(b) where the final masses of the stars are shown as black (present models) and gray (SWH18) dots. Since most of the mass is lost during the H and He burning phases, the scatter present in the SWH18 models cannot depend on the advanced

burning phases, but on something occurring in the H/He burning. The authors discuss this point and state that this "noise" is due to the effect of semiconvection in the central He burning that alters the surface properties of the stars and hence the mass-loss rate. Note that such a "noise" leads to quite a large scatter in the final total mass for stars more massive than 17 $M_\odot$ or so, and also to some scatter in the amount of ^{12}C left by the He burning. We cannot comment further on this point, apart from noting that semiconvection in central He burning is very effective in low mass horizontal branch stars, and that it progressively becomes less important as the initial mass increases. Above $\sim$10 $M_\odot$ or so, semiconvection should be negligible because of the progressive reduction of the dependence of the opacity on the C/He ratio (Castellani et al. 1985). Instabilities that lead to the ingestion of fresh He in the core (usually referred to as breathing pulses; Castellani et al. 1985) may occur but are spurious phenomena, at least in the massive stars regime, that may be easily cured by a proper choice of rezoning and the time step. Very recently, Woosley (2019), hereafter W19, published a large set of models of bare He cores and his Figure 11 shows the amount of ^{12}C left by the He burning as a function of the He core mass. The setup of these computations is the same adopted by SWH18. Since, as we already discussed above, the final amount of C left by He burning basically depends on just the He core mass during the latest phases of the He burning, and not on the previous history of the star, it is meaningful to plot the results from W19 in Figure 10(c). The green dots represent the values obtained by W19, and they are in excellent agreement with our three models computed with the same $^{12}C(\alpha,\gamma)^{16}O$ cross section adopted in the *Kepler* code.

In addition to the final total mass, Figure 10(b) also shows a comparison between the He core masses, the CO core masses, and the O-burning shell masses. The blue, red, and green dots refer to our models while the cyan, magenta, and dark green dots refer to the models from SWH18. Note that while the He and CO core masses of SWH18 show almost straight trends, our models bend slightly above 22 $M_\odot$ or so. The reason for this is that stars more massive than 22 $M_\odot$ lose not only their H-rich mantle but also part of their He core mass. Since He burning depends on the He core mass, the final CO core mass also shows an analogous bend. Our models have He core masses systematically larger than the predicted SWH18 ones: this result is very probably connected to different choices for the determination of the border of the convective core in H/He burning. The actual size of the convective core (and convective shells) is still subject to serious uncertainties, so different choices are equally plausible. The run of the CO core masses versus the initial mass, and vice versa, are in quite good agreement (apart from the more massive ones where the erosion of the He core due to mass loss induces the bending already discussed above), but this means that the He core mass–CO core mass relation is quite different between the two sets of models. To better highlight the differences between the two $M_{CO}(M_{He})$ relations, Figure 10(d) shows our relation as red dots and the SWH18 one as blue dots.

Since the fractions of ^{12}C left by He burning and M_{CO} are the key parameters that drive all of the advanced burning phase, the differences highlighted in Figures 10(c) and (d) between the two sets of computations clearly indicate how difficult it is to compare the final compactness predicted by the two sets of models. Therefore we simply show in Figures 10(e) and (f) a
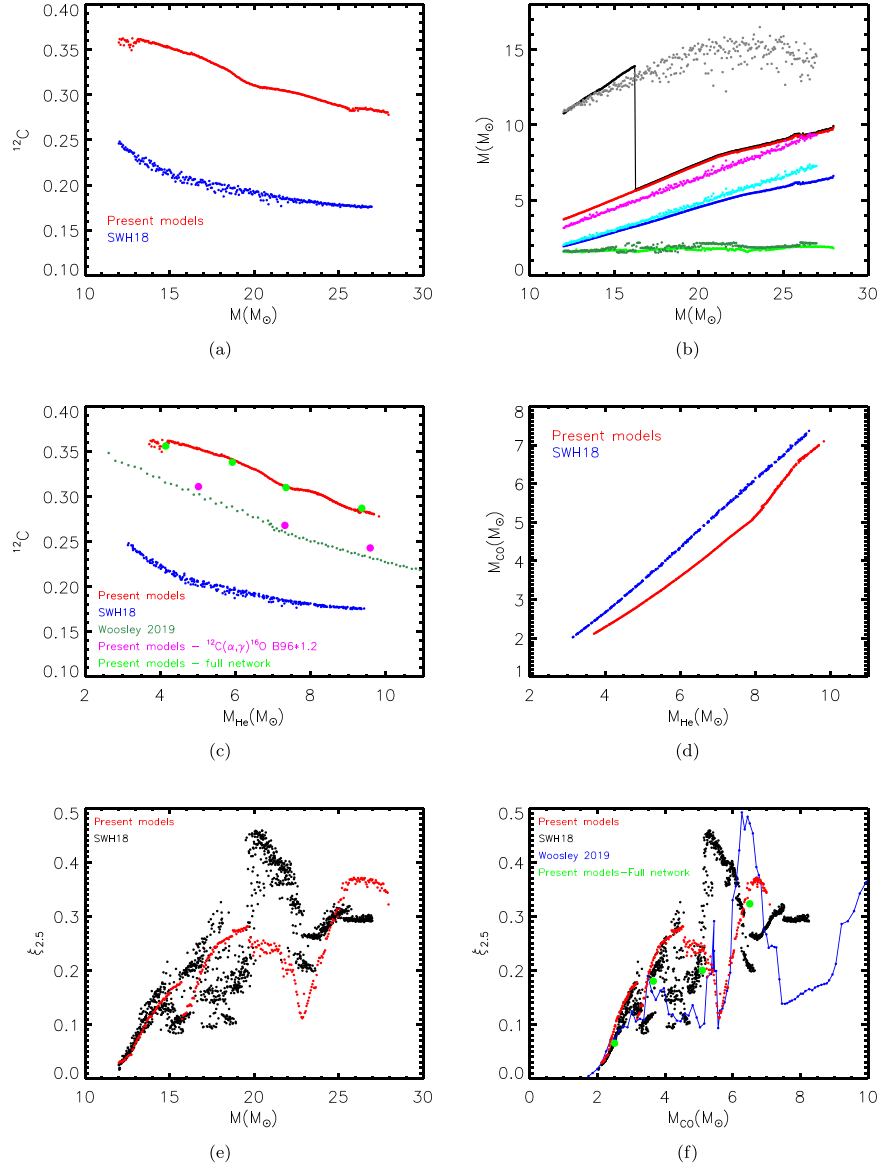
Figure 10. Comparison between some properties of our models and those of other similar computations available in the literature. Panel (a) shows the fraction of carbon left by He burning in our models (red dots) and in those of SWH18 (blue dots). Panel (b) shows the total mass, the He core mass, the CO core mass, and the O-burning shell mass. The respective color coding for our models is black, red, blue, and green, while the corresponding coding for the SWH18 models is gray, magenta, cyan, and dark green. (c) Same as (a) but with the addition of models published by Woosley (2019) and a few test models (see the text). (d) Comparison between the $M_{CO}(M_{He})$ relations of the present models and those of SWH18. (e) Comparison between the final compactness (computed for the mass coordinate $M = 2.5 \, M_\odot$) of our (red dots) and SWH18's (black dots) models. (f) Same as (e) but with the addition of the models by Woosley (2019; blue dots and line) and a few test models (see the text).

global comparison between the final $\xi_{2.5}$ values: (e) shows the comparison as a function of the initial mass while (f) shows the same comparison as a function of the CO core mass. The red and black dots refer to our and SWH18's models, respectively. As expected, the differences are quite large. Since the nonmonotonic average trend reflects the complex interplay among the various convective episodes, different combinations of CO core masses and ^{12}C abundances at the beginning of the advanced burning phases may easily lead to differences of the order of those shown in Figure 10. However, it is worth noting that our results do not show any significant scatter around the main trend. This trend is very well defined and all the features shown by our models are well understood and discussed in Section 3. A closer look at Figure 10(f) shows that SWH18's and our models share some similarities. The compactness of the

stars of lower mass, i.e., those having CO core masses up to, roughly, 3 $M_\odot$ is remarkably similar. The sharp discontinuity present in our models (largely discussed in Section 3) at $M_{CO} \sim 3.3 \, M_\odot$ ($M_{ini} = 15.75 M_\odot$) is not present in SWH18's models that, on the contrary, show a large scatter in this mass interval. However, note that a group of their models with low compactness clumps close to the position where our models show the discontinuity in the compactness $\xi_{2.5}$. We will not attempt any further analysis because the large differences in the initial conditions at the beginning of the advanced burning phases prevent a reliable quantitative understanding of the different predictions. Since the models computed by W19 also provide their final compactness, we also show their models in Figure 10(f). These models are particularly useful because they present the carbon mass fraction as intermediate between those

obtained by us and those obtained by SWH18 (see above). The ξ values of the models from W19 are shown as blue dots connected by a blue line to increase visibility. There are obviously large differences because in any case the C mass fractions at the beginning of the advanced burning phases are significantly different, but there are also striking similarities. In particular, ξ for both of the models in the low tail of the CO core mass (between, say, 1.5 and 3 $M_\odot$) is remarkably similar (among all three sets of models), and the well-shaped minimum is around 5.5 $M_\odot$. Also, the maximum at 6/6.5 $M_\odot$ is quite similar, even if the peak present in the models from W19 is higher. The formation of a higher peak agrees with the general expectation that the lower the C mass fraction, the lower the efficiency of the C convective shell (the third one), and the more compact the star.

Before closing this section we want to mention a few tests we made to check the role played by the adoption of a small network instead of our usual very extended one (Limongi & Chieffi 2018). Though the amount of computer time necessary to run all these models with the full network is prohibitive for us, we computed four models (13, 18, 20, and 26 $M_\odot$) with the full network. Note that our network (whichever the size) is always fully coupled to physical evolution and chemical mixing so that just one system of equations is solved in each time step. In particular, the system is formed by (4 + number of isotopes) × (number of meshes), which means more that 1.5 million equations are solved simultaneously for a network of 300 nuclear species and 5000 meshes. The large green dots in Figures 10(c) and (f) show the C mass fraction left by He burning and the final compactness of these four refined models. These tests quite convincingly show that the adoption of an extended, refined network does not qualitatively change the compactness obtained by means of a small network.

5. Conclusions

In this paper, we presented a very fine grid (in mass) of models in the range 12–27.95 $M_\odot$ in order to look at the fine structure of the relation between initial mass and final compactness of the models. The evolution beyond central He burning is biparametric because it depends on two parameters, the CO core mass and the fraction of C left by He burning. In principle, these two parameters are fully coupled (in nonrotating stars) and not independent but in practice, given the different prescriptions adopted by different groups in both managing convection and in the choice of the nuclear reaction rates, in the literature there are different pairings of CO core masses and the amount of C left by He burning. Our models show that the compactness of a star, $\xi_{2.5}$, is strictly connected to the behavior, birth, growth, overlap, and death of the various C convective episodes. The relation $\xi_{2.5}(M_{CO})$ is not a monotonic function of the CO core mass but shows features that are well understood and discussed. Moving from the low to the massive CO cores, a first drastic change in the behavior of $\xi_{2.5}$ occurs at $M_{CO} \sim 3\ M_\odot$; the reason being that stars having CO core masses up to 3 $M_\odot$ or so must wait for the disappearance of the second C convective shell before they can ignite Ne in the center. CO core masses above 3 $M_\odot$ are able to contract freely toward the Ne ignition independently of the ignition of the second C convective shell. As a consequence, the second C convective shell ignites more violently that in the smaller masses, causing the expansion of a large fraction of the mass

above it. As the CO core mass increases, the strength of the second C convective shell progressively weakens (because of the inverse scaling of the fraction of C left by He burning with the CO core mass) and the compactness of the star progressively increases again. However, as the CO core mass increases further, a second jump appears at a CO core mass of the order of 4.6 $M_\odot$. This second jump is due to the progressive weakening of the efficiency of the second C convective shell that favors the contraction of the overlying mass and hence an early ignition of the third C convective shell. The net consequence is that the layers above this newly born C convective shell react by expanding and hence induce a reduction of the compactness $\xi_{2.5}$. As the CO core mass continues to increase, the compactness starts rising again because the strength of the third C convective shell progressively weakens as a consequence of the progressive lower C abundance left by the He burning.

Let us finally stress again that all the features of the $\xi_{2.5}(M_{CO})$ relation discussed above depend on the ^{12}C(M_{CO}) relation, and therefore they can vary, even significantly, from one author to another. However, in spite of the complex interplay among the various C convective episodes that sculpt the dependence of the compactness of a star on the CO core mass, our models do not show any evidence of a significant scatter of the data: the relation is very tight and well defined.

ORCID iDs

Alessandro Chieffi ⬡ https://orcid.org/0000-0002-3589-3203
Marco Limongi ⬡ https://orcid.org/0000-0003-0636-7834

References

Angulo, C., Arnould, M., Rayet, M., et al. 1999, NuPhA, 656, 3
Arnett, W. D. 1983, ApJL, 263, L55
Asplund, M., Grevesse, N., Sauval, A. J., & Scott, P. 2009, ARA&A, 47, 481
Baron, E., Cooperstein, J., & Kahana, S. 1985, NuPhA, 440, 744
Bethe, H. A. 1990, RvMP, 62, 801
Buchmann, L. 1996, ApJL, 468, L127
Buchmann, L. 1997, ApJL, 479, L153
Burrows, A., Radice, D., Vartanyan, D., et al. 2019, MNRAS, 485, 3153
Castellani, V., Chieffi, A., Pulone, L., & Tornambe, A. 1985, ApJ, 296, 204
Chieffi, A., Limongi, M., & Straniero, O. 1998, ApJ, 502, 737
Cooperstein, J., Bethe, H. A., & Brown, G. E. 1984, NuPhA, 429, 527
Ertl, T., Janka, H.-T., Woosley, S. E., et al. 2016, ApJ, 818, 124
Imbriani, G., Limongi, M., Gialanella, L., et al. 2001, ApJ, 558, 903
Janka, H.-T. 2017, ApJ, 837, 84
Kunz, R., Fey, M., Jaeger, M., et al. 2002, ApJ, 567, 643
Limongi, M., & Chieffi, A. 2012, ApJS, 199, 38
Limongi, M., & Chieffi, A. 2018, ApJS, 237, 13
Müller, B., Melson, T., Heger, A., et al. 2017, MNRAS, 472, 491
O'Connor, E., & Ott, C. D. 2011, ApJ, 730, 70
O'Connor, E., & Ott, C. D. 2013, ApJ, 762, 126
Sukhbold, T., & Woosley, S. E. 2014, ApJ, 783, 10
Sukhbold, T., Woosley, S. E., & Heger, A. 2018, ApJ, 860, 93
van Loon, J. T., Cioni, M.-R. L., Zijlstra, A. A., & Loup, C. 2005, A&A, 438, 273
Woosley, S. E. 2019, ApJ, 878, 49